Numerical investigation into the blasting-induced damage characteristics of rocks considering the role of in-situ stresses and discontinuity persistence

L.B. Jayasinghe, Junlong Shang†, Zhiye Zhao, A.T.C. Goh,

Nanyang Centre for Underground Space, School of Civil and Environmental Engineering, Nanyang Technological University, Singapore 639798.

†Corresponding author: shangjunlongcsu@gmail.com, jlshang@ntu.edu.sg (J. Shang)

ABSTRACT

This paper presents a 3D coupled Smoothed Particle Hydrodynamics (SPH) and Finite Element Method (FEM) model, which was developed to investigate the extent of damage zone and fracture patterns in rock due to blasting. The RHT material model was used to simulate the blasting-induced damage in rock. The effects of discontinuity persistence and high in-situ stresses on the evolution of blasting-induced damage were investigated. Results of this study indicate that discontinuity persistence and spatial distribution of rock bridges have a significant influence on the evolution of blasting-induced damage. Furthermore, high in-situ stresses also have a significant influence on the propagation of blasting-induced fractures, as well as the patterns of fracture networks. It is also shown that the blasting-induced cracks are often induced along the direction of the applied high initial stresses. Moreover, additional cracks are normally generated at the edges of the rock bridges probably due to the relatively high stress concentration.

Keywords: Blasting; Rock damage; In-situ stress; Discontinuity persistence; RHT model

1. Introduction

Blasting-induced damage characteristics of rocks is not well understood due to the complex interaction between the blasting induced shock wave and ubiquitous rock discontinuities. An improper blast design may result in inadequate rock fragmentation, or cause unwanted damage of the surrounding rocks or structures, leading to safety and instability issues and economic loss [1-4]. In practice, approximate methods based on experience are mostly used in the prediction and control of blast damage. However, it is necessary to have a better understanding of the nature and extent of the rock damage caused by blasting to achieve an optimum blasting design by avoiding the negative consequences.

Rock blasting leads to the mechanical deterioration of rock masses and, in particular, results in the opening, loosening and propagating of pre-existing rock discontinuities, as well as the generation of new cracks in rock matrix by the combined actions of the stress wave and the gas pressure. In the process of rock fragmentation by blasting, stress wave is mainly responsible for the initiation of the initial radial fracture network, while the explosion gas pressure further extends the cracks towards the rock fragmentation [5-8].

Numerical approaches provide a tool to investigate the mechanisms of rock blast safely and in detail. Finite element method (FEM) has become one of the promising numerical approaches to study the blasting-induced damage characteristics of rocks. Ma and An [9] investigated the influence of pre-existing joints, loading rate and in-situ stress on the damage characteristics of rock masses under blasting using a two-dimensional FEM model. They found that the fractures induced by blasting were oriented in the direction of the maximum in-situ stress. By using a coupled FEM-DEM approach, the dynamic rock fracturing process of jointed rock masses under blasting was numerically investigated by Wang and Konietzky [10], who concluded that the existence of in-situ stress field caused the non-uniformity of rock fracture. However, no plastic crushed zone was observed in their study because the rock mass was assumed to be elastic. Zhu et al. [11] developed a FEM model for understanding the blasting-induced damage in cylindrical rocks. The effects of loading rate and anisotropic high in-situ stresses on blasting performance and blast-induced damage zones was explored by Yilmaz and Unlu [12] through a 3D FLAC analysis. Zhao et al. [13] studied the blasting-induced fracture expansion of bedded coal using the isotropic and kinematic hardening plasticity material model in LS-DYNA. It was noticed that the distance from the bedding plane and the borehole has a significant influence on fracture patterns. Yi et al. [14] used a 2D plane strain model to investigate the effect of in-situ stresses on the fracturing of rock due to blasting.

In previous studies, 2D plane strain models with an equivalent blast pressure were often used to investigate the crack initiation and propagation in blasting under in-situ stresses. Those 2D analyses, however, cannot incorporate the three-dimensional propagation of the energy from the detonation of explosives. Also, it cannot simulate the vertically propagation of the Swaves from the borehole. Therefore, a three-dimensional model that can consider the explosive charge length and the detonation velocity of the explosive will offer more realistic results.

Additionally, the impact of the areal persistence, which can reflect the three dimensional nature of rock discontinuities, on the evolution of blasting-induced characteristics is still not well understood. In previous numerical studies, trace length (2D) is often used as an approximation of the 3D areal persistence, and sometimes persistence was conservatively assumed to be 100%, which will inevitably result in a wrong prediction of failure mechanism or fragmentation of rocks [15, 16].

The objective of this work is to investigate the effects of in-situ stresses and discontinuity persistence on the blasting-induced damage characteristics of rocks by using a three-dimensional numerical approach. To avoid time-consuming computation, the Smoothed Particle Hydrodynamics (SPH) and Lagrangian FEM mesh is coupled in the study to maintain a good computational efficiency, which will be described in Section 2. In what follows, a brief description of the background on modelling is presented. Then, the calibration and validation of the model parameters to simulate the blasting-induced rock damage are presented. Subsequently, the effects of discontinuity persistence and high in-situ stresses on the damage zone and fracture patterns in rock due to blasting are investigated, followed by the results interpretation, discussion, and conclusion of the study.

2. Numerical model set-up

In this study, the commercial software LS-DYNA [17] and the Riedel-Hiermaier-Thoma (RHT) model [18] was used to simulate the damage evolution of rock mass under blasting load. The detonation of the explosive was directly modelled with the high explosive burn material model with Jones-Wilkins-Lee (JWL) equation of state in LS-DYNA.

2.1 Rock material model

LS-DYNA contains several material models that can be used to represent damage evolution of rock under blasting. The RHT material model, which is capable of characterising rock mass behaviour under high strain rate blast loads, was used in this study. It is an advanced plasticity model for brittle materials such as concrete and rocks. Literature has shown that the RHT material model can successfully incorporate non-linear rock properties [14, 19-21].

In the RHT model, the strength model is described using the three limit surfaces in stress space, namely the initial elastic yield surface, the failure surface and the residual surface which consider pressure and strain rate. This model also considers the effect of strain hardening and damage softening to characterise the post-yield and post-failure behaviours [22].

The failure surface, σ_f, describes the maximum distortion stress that the material can withstand and it is expressed as,

$$\sigma_f = f_c \sigma_f^* \left(p^*, F_r\left(\dot{\varepsilon}_p, p^*\right)\right) R_3(\theta, p^*) \tag{1}$$

where θ is Lode angle, $\dot{\varepsilon}_p$ is the effective plastic strain rate and p^* is the normalized pressure to the unconfined uniaxial cylindrical compressive strength, f_c. The factor R_3 is introduced to account for the reduced strength on shear and tensile meridians. F_r is the dynamic strain rate increase factor and it is defined by Eqs. (2) to (4).

$$F_r\left(\dot{\varepsilon}_p, p^*\right) = \begin{cases} F_r^c & 3p^* \geq F_r^c \\ F_r^c - \frac{3p^* - F_r^c}{F_r^c + F_r^t f_t^*}\left(F_r^t - F_r^c\right) & F_r^c > 3p^* \geq -F_r^t f_t^* \\ F_r^t & -F_r^t f_t^* > 3p^* \end{cases} \tag{2}$$

$$F_r^{c,t}\left(\dot{\varepsilon}_p\right) = \begin{cases} \left(\frac{\dot{\varepsilon}_p}{\dot{\varepsilon}_0^{c,t}}\right)^{\beta_{c,t}} & \dot{\varepsilon}_p \leq \dot{\varepsilon}_p^{c,t} \\ \gamma_{c,t} \sqrt[3]{\dot{\varepsilon}_p} & \dot{\varepsilon}_p > \dot{\varepsilon}_p^{c,t} \end{cases} \tag{3}$$

$$log\, \gamma_c = 6\beta_c - 0.492; \quad log\, \gamma_t = 7\beta_t - 0.492 \tag{4}$$

In the above equations, c and t (subscripts and superscripts) denote compression and tension, respectively. β_c and β_t are the compressive and tensile strain rate dependence exponents, respectively, and f_t^* denotes the normalized tensile strength to the compressive strength, f_c.

The initial elastic surface, σ_{el}, is derived from the failure surface, σ_f, using the elastic strength parameter, F_e, and the cap function, F_c, as given in Eq. (5).

$$\sigma_{el} = f_c \sigma_f^* \left(\frac{p^*}{F_e}, F_r\left(\dot{\varepsilon}_p, p^*\right)\right) R_3(\theta, p^*) F_e(p^*) F_c(p^*) \tag{5}$$

When the stress states reach the failure surface, the damage from the plastic strain accumulates as:

$$D = \sum \frac{\Delta\varepsilon_p}{\varepsilon_p^f}; \qquad \varepsilon_p^f = D_1(p^* - (1-D)p_t^*)^{D_2} \geq \varepsilon_{f,min} \tag{6}$$

where D is the damage, ranging from 0 (undamaged) to 1 (fully damaged), $\Delta\varepsilon_p$ is the accumulated plastic strain, ε_p^f is the equivalent plastic strain at failure, p_t^* is the normalized failure cutoff pressure (often denoted as Hugoniot Tensile Limit) and $\varepsilon_{f,min}$ is the minimum allowable plastic strain. D_1 and D_2 are the constants.

After damage begins to accumulate, the failure surface starts soften and then the residual surface, σ_r, is defined as:

$$\sigma_r^*(p^*) = \begin{cases} A_f p^{*n_f} & p^* > 0 \\ 0 & p^* \leq 0 \end{cases} \tag{7}$$

where A_f and n_f are the constants. A detailed description of the RHT material model can found in Borrvall and Riedel [22].

2.2 Blasting load

In numerical simulations, blast loads can be directly applied on the borehole wall as a blast pressure curve can be calculated using empirical equations [23-25]. On the other hand, the blast loads can also be generated by the explosive charge that can be simulated using high explosive burn material model with the JWL equation of state (EOS) in LS-DYNA. The JWL EOS defines the pressure as a function of the relative volume, V and internal energy, E, which can be expressed as [17]

$$P = A\left(1 - \frac{\omega}{R_1 V}\right)e^{-R_1 V} + B\left(1 - \frac{\omega}{R_2 V}\right)e^{-R_2 V} + \frac{\omega E}{V} \tag{8}$$

where A, B, R_1, R_2 and ω are the material constants.

A factor called burn fractions, F, is used in the high explosive burn material model to control the chemical energy release for detonation simulations, and it is calculated as [17]

$$F = \max(F_1, F_2) \tag{9}$$

$$F_1 = \begin{cases} \frac{2(t - t_l)D}{3\Delta x} & if\ t > t_l \\ 0 & if\ t \leq t_l \end{cases} \tag{10}$$

$$F_2 = \frac{1-V}{1-V_{cj}} \quad (11)$$

where D is the detonation velocity, ρ is the density, V_{cj} is the Chapman-Jouget relative volume, V is the relative volume, t_l is initiation time, t is the current time and Δx is the characteristic length of an element [17].

2.3 Model parameters and validation

The results of the laboratory-scale explosion tests in Banadaki [26] were used to calibrate the RHT model and verify the simulation results of this study. Banadaki [26] conducted 30 laboratory-scale explosion tests on two different types of cylindrical rock samples (Laurentian granite and Barre granite). In this study, the results based on the Barre granite were chosen in the comparison study. The cylindrical Barre granite sample has a diameter of 144 mm and a height of 150 mm, with a 6.45 mm diameter blasthole in the middle as shown in Fig. 1(a). A copper tube with 1.2 mm thick was installed in the blasthole to prevent gas penetration into the cracks.

As mentioned earlier, in our simulations, a 3D coupled Smoothed Particle Hydrodynamics and Finite Element Method (SPH-FEM) model is established to investigate the failure mechanisms of rocks under blast loading. The use of the conventional Lagrangian meshes in the large deformation problems will result in mesh tangling, leading to severe numerical instabilities. SPH is a mesh-free Lagrangian method which employs a finite number of particles that carry individual mass to represent the material and form the computational domain. SPH method has a solid ability to deal with dynamic large deformation problems, due to its ability to handle large distortions by avoiding mesh tangling and remeshing. Although SPH has great advantages in simulating many problems in engineering and science, SPH is much expensive in terms of computation time (especially for 3D model). Because a large number of small particles would be required and the time step would become very small. Thus, coupling the SPH and Lagrangian FEM mesh is a potentially right solution to overcome the element distortion, and as well as to maintain good computational efficiency. In this study, SPH algorithm was implemented in LS-DYNA to model the detonation of PETN explosive, and the Lagrangian meshes were used to model the rock and copper tube as shown in Fig. 1(b). The procedure of the RHT model parameter selection has been presented in detail in Xie et al. [19]. The model parameters were adjusted by conducting sensibility analysis. The RHT model parameters for Barre granite are listed in Table 1. The parameters for the PETN explosive are summarized in Table 2. The plasticity kinematic material model was used to model the copper tube, and the material parameters for the copper are given in Table 3.

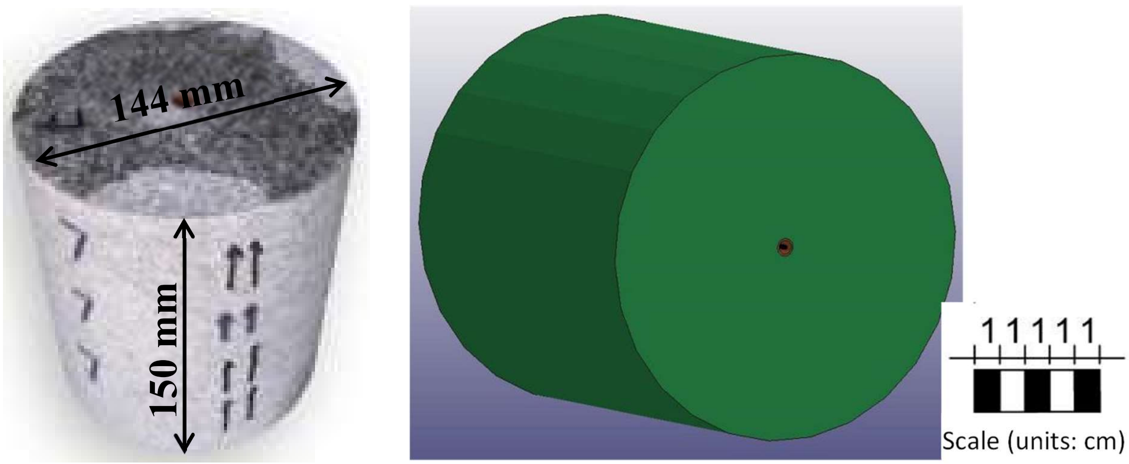

(a) (b)

Fig. 1. Cylindrical Barre granite samples. (a) Blast experiment [26] and (b) 3D numerical model.

Table 1. Material parameters for rock

Parameter	Value	Parameter	Value	Parameter	Value
RO (kg/m^3)	2660	T2	0	EPM	0.01
SHEAR (GPa)	21.9	E0C	$3x10^{-8}$	AF	0.25
EPSF	2	E0T	$3x10^{-9}$	NF	0.62
B0	1.22	EC	$3x10^{22}$	GAMMA	0
B1	1.22	ET	$3x10^{22}$	A1 (GPa)	25.7
T1 (GPa)	25.7	BETAC	0.032	A2 (GPa)	37.84
A	2.44	BETAT	0.036	A3 (GPa)	21.29
N	0.76	PTF	0.001	PEL (MPa)	125

FC (MPa)	167.8	GC*	1	PCO (GPa)	6
FS*	0.18	GT*	0.7	NP	3
FT*	0.05	XI	0.5	ALPHA	1
Q0	0.567	D1	0.04		
B	0.01	D2	1		

Table 2. Material and JWL EOS parameters for PETN [26]

Density (kg/m^3)	Velocity of detonation (m/s)	P_{CJ} (GPa)	A (GPa)	B (GPa)	R_1	R_2	ω	E_0 (GPa)
1320	6690	16	586	21.6	5.81	1.77	0.282	7.38

Table 3. Material parameters for copper [27]

Density (kg/m^3)	Young's modulus (GPa)	Poisson's ratio	Yield stress (MPa)	Tangent modulus (MPa)	β	C (s^{-1})	P
8930	117	0.35	400	100	0	1.346×10^6	5.286

Figs. 2 and 3 show comparisons of the blasting-induced crack patterns obtained from experiment [26] and the results of the present 3D numerical model. In the numerical results, the cracks are shown by the damage contours which range from 0 to 1. The blue colour represents the fringe level 0 which indicates the undamaged rock, while the red colour represents the fringe level 1 which indicates the rock is completely damaged. The other colours which are associated with fringe levels between 0 and 1 represent the different damage levels of the rock.

It can be seen from Figs. 2 and 3 that the results of our 3D model match well with that obtained from experiment. Basically, crush zones are generated around the blastholes and radial cracks propagate towards the outer boundaries from the blastholes when the detonation is occurred. In addition, a few circumferential cracks can be seen close to the boundary of the sample at the bottom surface. The intensity of cracks at the bottom surface of the rock sample is much higher than that observed at the top surface, which is due to the effect of the superposition of stress wave. The observed reasonable predictions of our 3D numerical model give us some confidence in its further application in the later study.

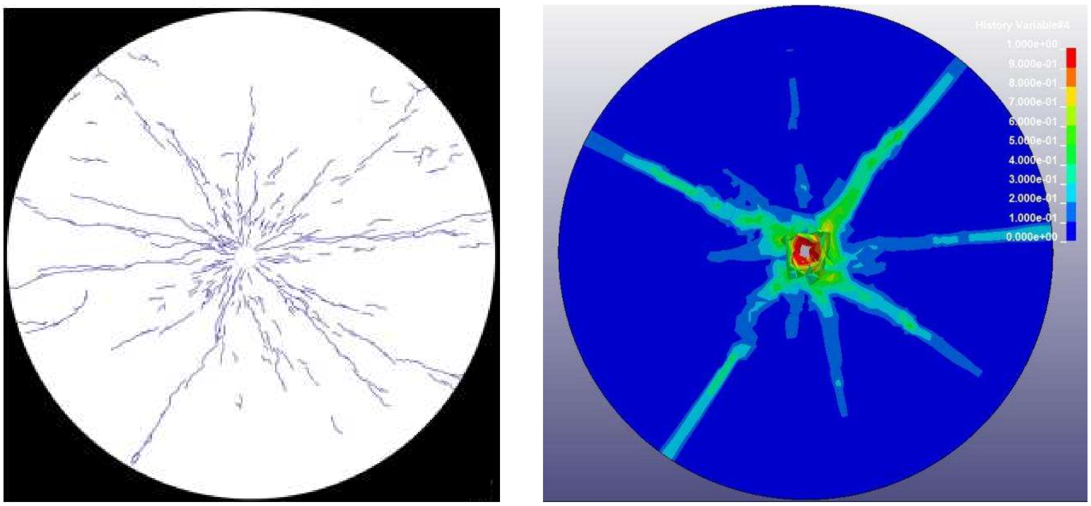

(a) (b)

Fig. 2. Comparison of blasting-induced crack patterns observed at the top surface of a cylindrical Barre granite sample. (a) Blast experiment [26] and (b) 3D numerical simulation.

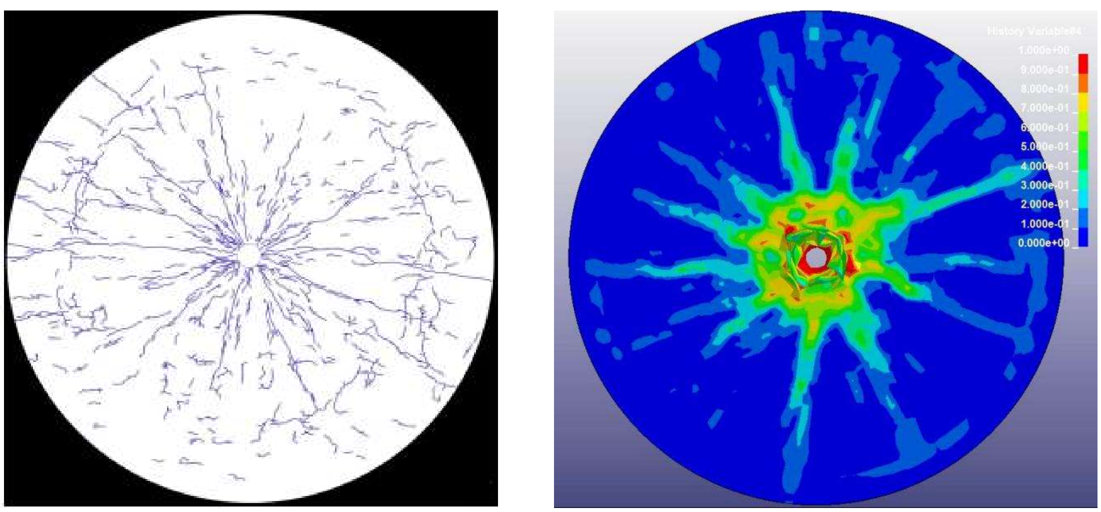

(a) (b)

Fig. 3. Comparison of blasting-induced crack patterns observed at the bottom surface of a cylindrical Barre granite sample. (a) blast experiment [26] and (b) 3D numerical simulation.

To further testify the generated 3D numerical model, the numerically and experimentally obtained maximum pressures measured at different distances from the borehole wall were compared (Fig. 4). The comparison shows that the present simulation results of pressure distribution match the test results quite well, which further validates the robustness of the proposed 3D SPH-FEM model.

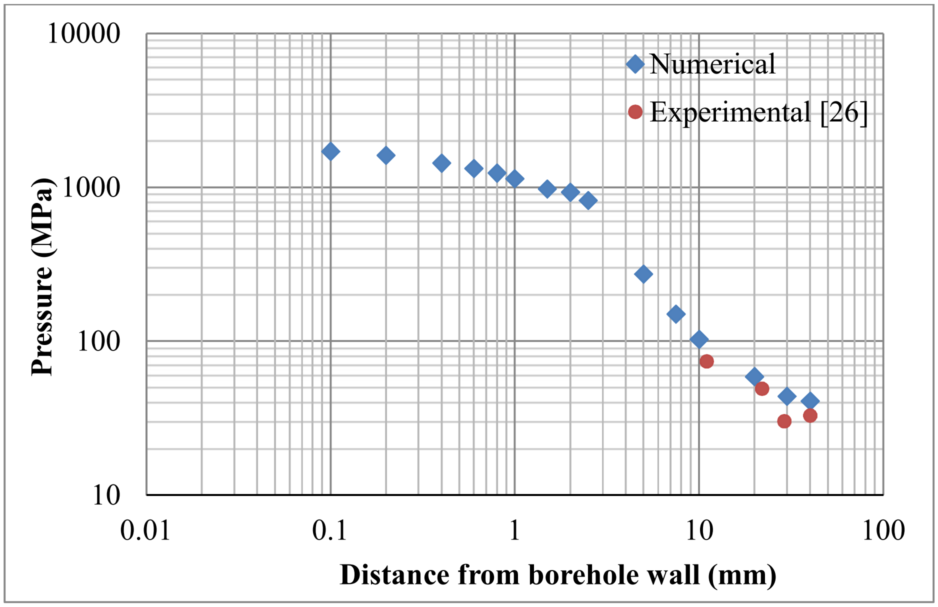

Fig. 4. Comparison of the numerically and experimentally obtained maximum pressures measured at different distances from the borehole walls.

3. Results and discussion

In this section, the results of the crack initiation and propagation due to blasting under various scenarios are presented. The influence of in-situ stresses and discontinuity persistence on the characteristics of the blasting-induced damage of rock mass are evaluated and discussed.

Fig. 5 shows the developed 3D SPH-FEM model to study the damage mechanisms of rock under blasting. The model is 4 m long, 4 m wide and 2 m high. The blasthole diameter and length are 50 mm and 0.5 m, respectively. The explosive charge was modelled with the SPH particles, while the rock was modelled with the Lagrangian meshes. The rock mass was modelled using RHT material model as described earlier. However, ANFO explosive was considered in these analyses and the parameters for the ANFO explosive are summarized in Table 4. The automatic node to surface contact conditions was used for the coupling interaction between the SPH particles and Lagrange solid elements. Non-reflecting boundaries were applied at the boundaries except the top surface which is free.

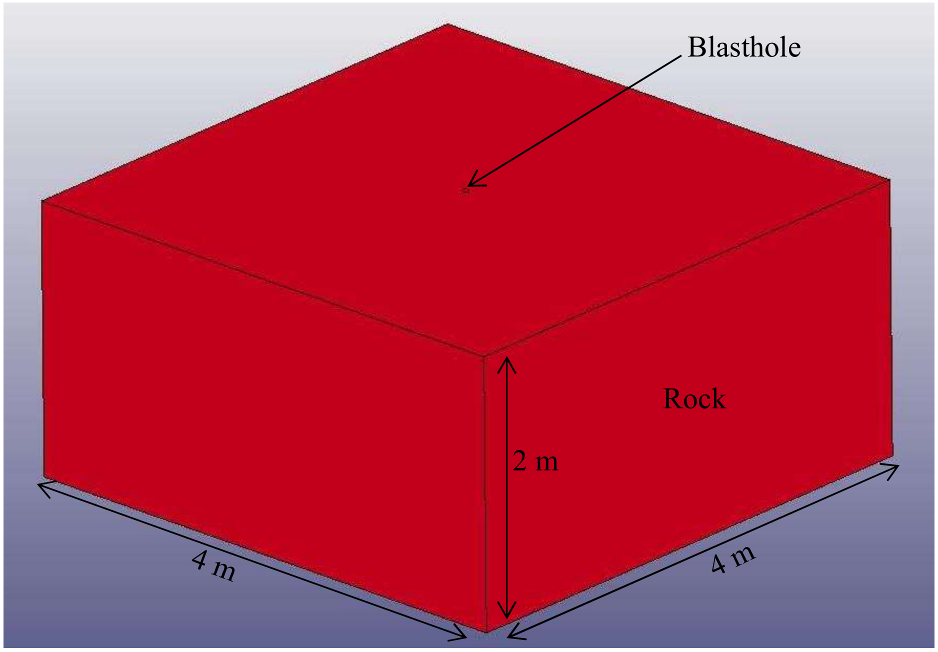

Fig. 5. 3D FE model

Table 4. Material and JWL EOS parameters for ANFO

Density (kg/m^3)	Velocity of detonation (m/s)	P_{CJ} (GPa)	A (GPa)	B (GPa)	R_1	R_2	ω	E_0 (GPa)
931	4160	5.15	49.46	1.891	3.907	1.118	0.333	2.484

3.1 Effect of in-situ stresses on blasting-induced fracture behaviour

The magnitude of in-situ stresses normally increase with the depth. High in-situ stresses at deeper depths can cause difficulties for excavation-related engineering activities such as deep tunnelling and mining. The effect of in-situ stresses on the fracturing of rock due to blasting has been investigated extensively, most of which however were based on the 2D plane strain models with an equivalent pressure-time history curve applied on the borehole wall [6, 9, 12, 14]. In this study, a 3D SPH-FEM coupled model combining blast loads and in-situ stresses is used, which is expected to realistically reflect the three-dimensional nature of the blasting-induced fracturing process in rocks. In order to assess the influence of in-situ stresses on fracture behaviour, four different analysis cases are considered as shown in Fig. 6 and Table 5. Fig. 6 shows the cross-sectional view of the established numerical model. The pressures P1 and P2 were applied to the outer vertical boundaries of the model, and the stress initialization to apply constant initial in situ stresses in the rock was first carried out by using the

*CONTROL_DYNAMIC_RELAXATION option in LS-DYNA. After the stress initialization, the detonation of the explosive was simulated, and the stress evolution in the rock and the initiation and propagation of blasting-induced cracks were monitored.

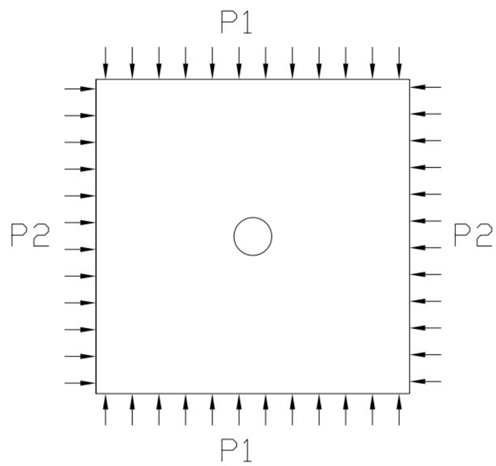

Fig. 6. Cross-sectional view of the established numerical model.

Table 5. Four analysis cases designed to understand the effects of in-situ stresses on fracture behaviour

Analysis case	P1 (MPa)	P2 (MPa)
I	0	0
II	60	60
III	60	30
IV	60	0

Fig. 7 illustrates the initiation and propagation of cracks around the blasthole at different times for case I. It can be seen that just after the detonation of the explosive initiated at the bottom of the blasthole, a crushed zone is first developed continuously around the blasthole as shown in Fig. 7(a). Then, radial cracks were induced by the tensile stress and propagated radially, as shown in Figs. 7(b) and (c). As can be seen in Fig. 7(c), the blasting damage of rock gradually evolved from the bottom of the blasthole to the top surface. As a result of the reflection of the stress wave at the top free surface and thus generation of excessive tensile stresses, the damage is more significant at the top surface.

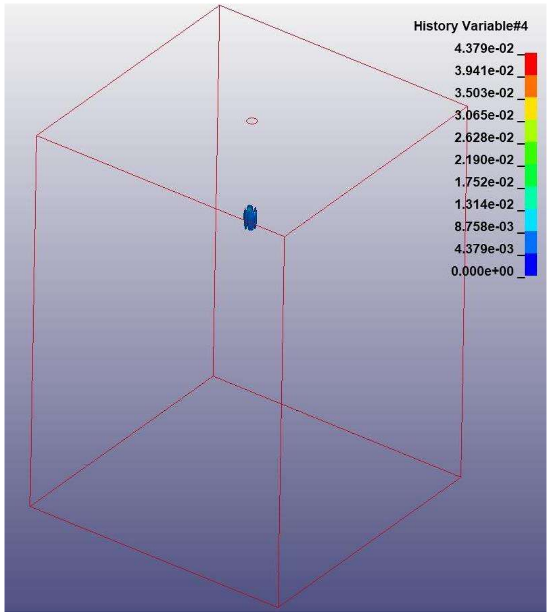

(a)

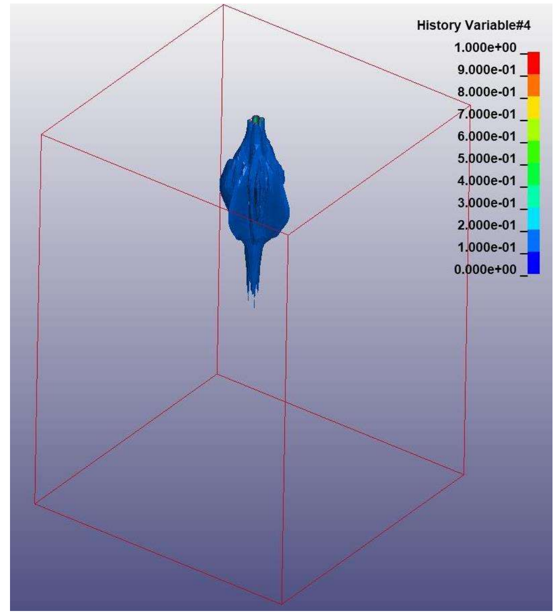

(b)

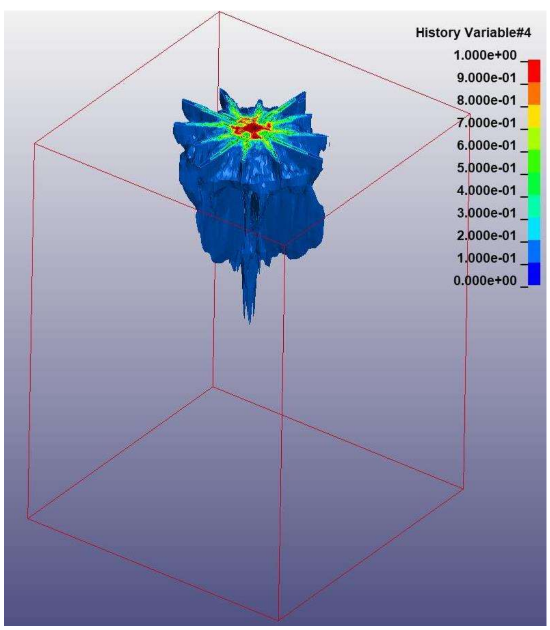

(c)

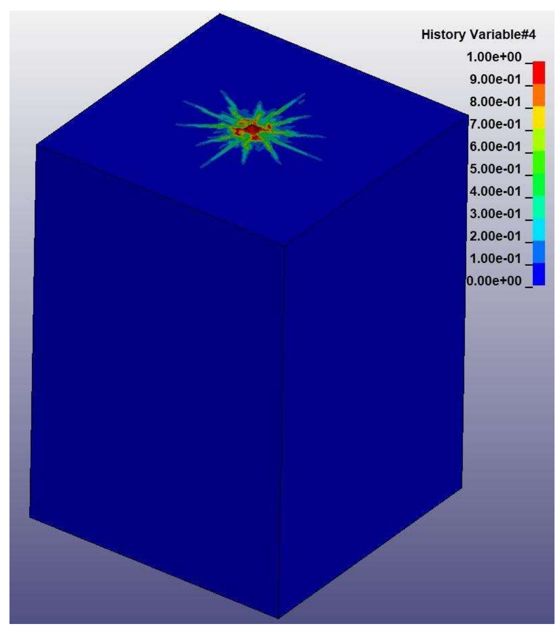

(d)

Fig. 7. Evolution of blasting-induced cracks at times. (a) 10 μs (b) 100 μs (c) 400 μs and (d) crack pattern at the top surface at 400 μs.

Fig. 8 shows a comparison of the blasting-induced rock damage on the top surface for all cases. The comparison of the results obtained in cases I and II shows that the rock mass without the influence of horizontal in-situ stresses (case I) exhibits more blasting-induced damage than the case with the consideration of horizontal in-situ stresses (case II). The extent of cracks is expected to decrease with increasing the lateral in-situ stresses, because the stress (or confinement) applied on the rock tends to resist the propagation of blasting-induced fractures. Also, it can be clearly seen that when there is an anisotropic in-situ stress field, the rock mass is subjected to anisotropic rock damage, and blasting-induced cracks are aligned in the direction of the major horizontal principal stress axis (i.e. the direction of P1 in this study). This is due to the suppression of the tensile stress in the direction of P2 under a higher P1. The results agree well with some numerical findings in literature [6, 9, 12, 14].

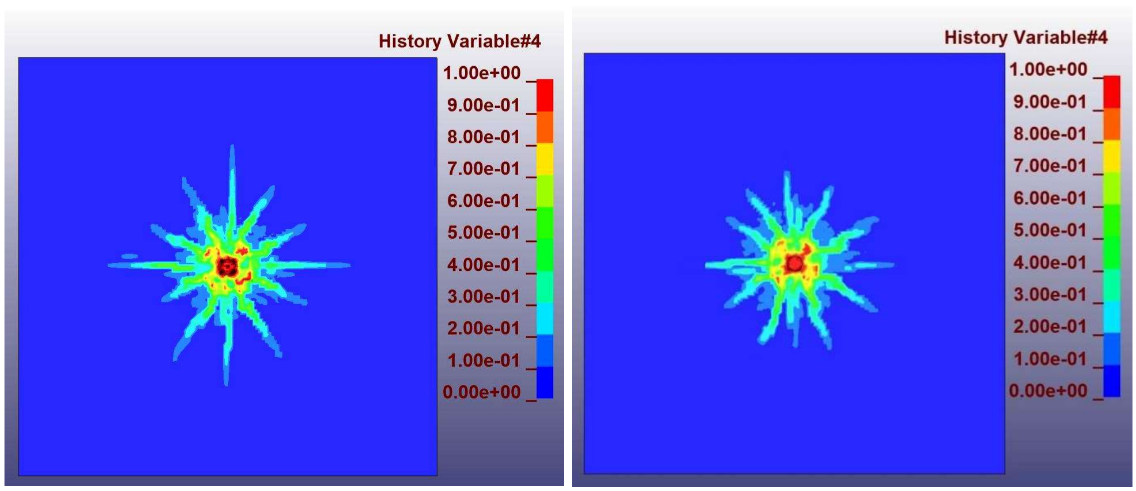

(a) (b)

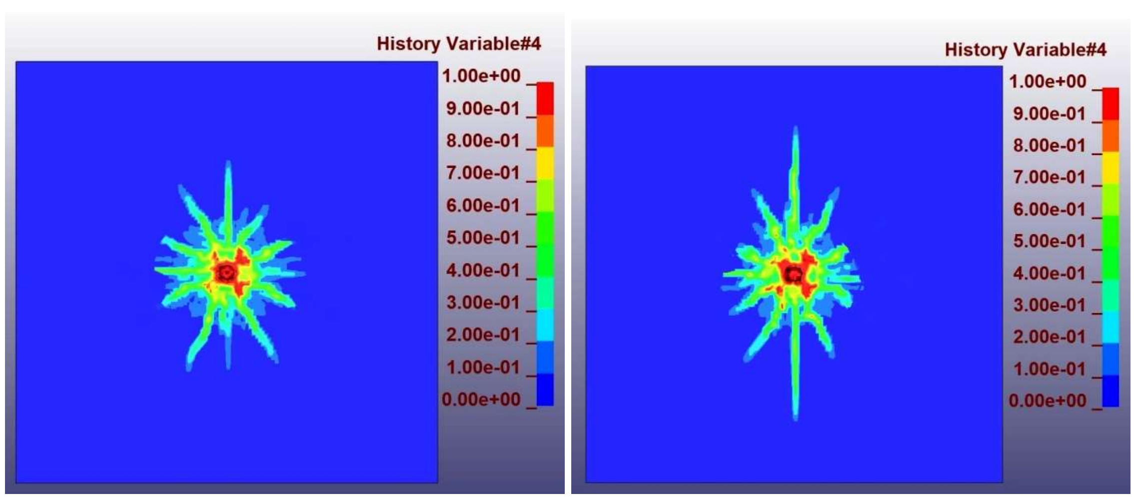

(c) (d)

Fig. 8. Crack patterns on the top surface for (a) case I (b) case II (c) case III and (d) case IV.

As stated above, there exist many 2D studies on the influence of in-situ stress on blast-induced rock cracks in literature. It is seen that the present 3D numerical results agree well with some of previous numerical findings. A comparison study was further carried out to understand the difference between the results from 3D and 2D simulations. The blasting-induced rock damage on the top surface obtained from the 2D and 3D models are compared in Fig. 9. Although the crack patterns are similar for both models, the blasting-induced rock cracks obtained from the 3D analysis are relatively larger, because of the effect of the stress wave superposition when the detonation wave propagation within the cylindrical charge. Within the acceptable computation time, the 3D model predicts the cracking behaviour more realistically, because it considers the explosive charge length and velocity of detonation of the explosive.

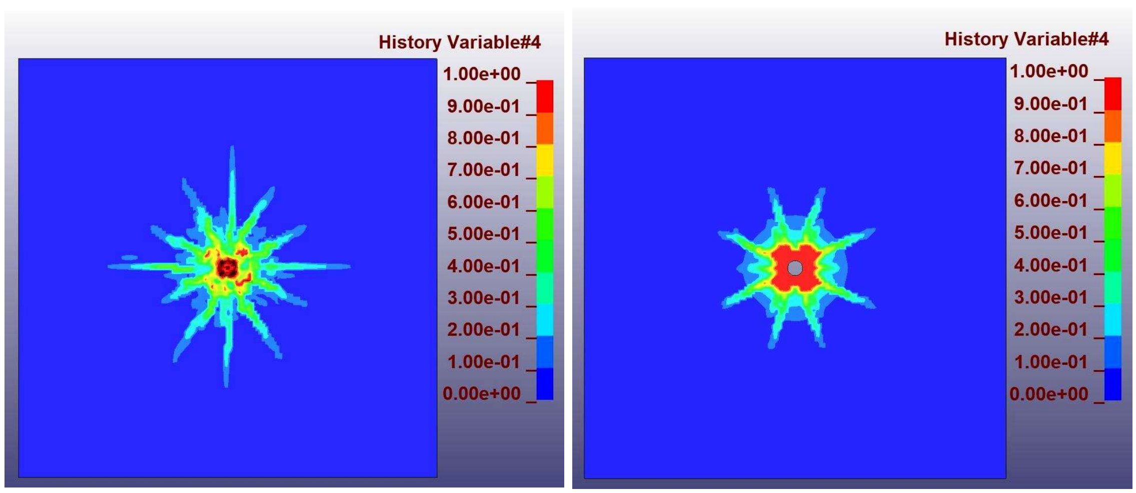

(a) (b)

Fig. 9. Crack patterns on the top surface from (a) 3D analysis and (b) 2D analysis.

3.2 The role of discontinuity persistence

Rock discontinuities are ubiquitous in nature, which can unavoidably influence the blasting-induced fracture propagation in natural rocks. The term discontinuity persistence, *k*, has been used to describe the areal extent of a rock discontinuity. It is defined as the fraction of continuous discontinuity area, as expressed by Eq. 12 [28].

$$k = \frac{A_j}{A_j + A_b} \tag{12}$$

where A_j is the total area of joints along the joint plane and A_b is the total area of rock bridges. The small area of intact rock separating coplanar or non-coplanar joints is defined as a rock bridge [29], which rock bridge plays an important role in stabilizing jointed rock masses [30, 31].

To assess the influence of discontinuity persistence and geometry of rock bridges on the blasting-induced fracture behaviour, four different cases are considered. Fig. 10 shows the configurations of the continuous joint segments (marked by "J") and rock bridges (marked by "R") along the joint plane for each analysis case. The discontinuity persistence varied from 0.18 to 0.36 in this study. The cases A and C have the persistence of 0.18 and for cases B and D it is 0.36 and 0.2, respectively. The distance to the joint plane from the blasthole was taken as 0.2 m. The continuous joint segments were simplified as flat gaps (or fissures) with a width of 2 mm and no filling material was considered in the simulations. A surface to surface contact type was applied to simulate the joint plane, without the need of assigning joint stiffness, roughness parameters. It is also assumed that the true cohesion of the continuous joint segments is negligible, because the tensile and shear strengths of the intervened rock bridges can be much larger than that of joint segments.

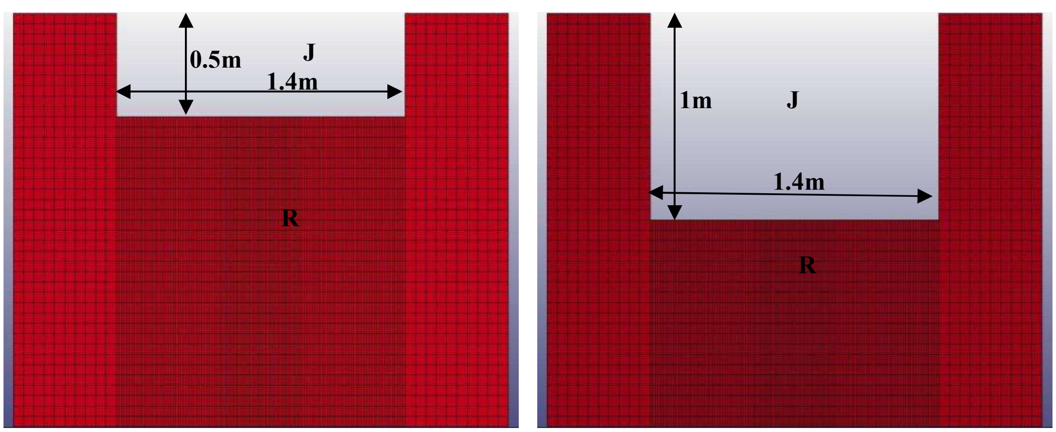

Case A Case B

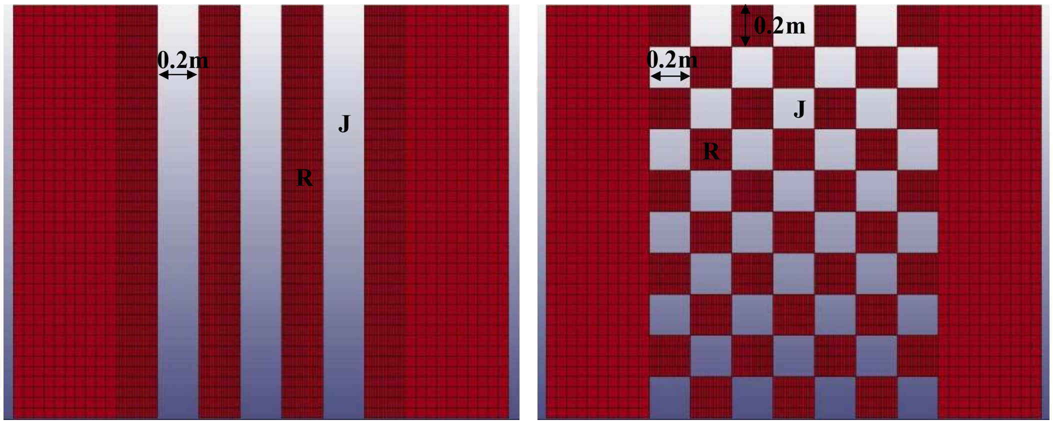

Case C Case D

Fig. 10. Analysis cases used for investigating the effect of discontinuity persistence on blasting-induced fracture behaviour.

The simulated fracture patterns and damage contours for case A are shown in Fig. 11. Many blasting-induced cracks were generated around the blasthole and in the region immediately around the joint plane, as shown in Fig. 11(a). No damage on the rock matrix can be seen beyond the joint plane in this case. The perspective view of blasting-induced damage on rock mass is shown in Fig. 11(b). Due to the significant stress concentration around the rock bridges, additional damage was created at the edges of the rock bridges

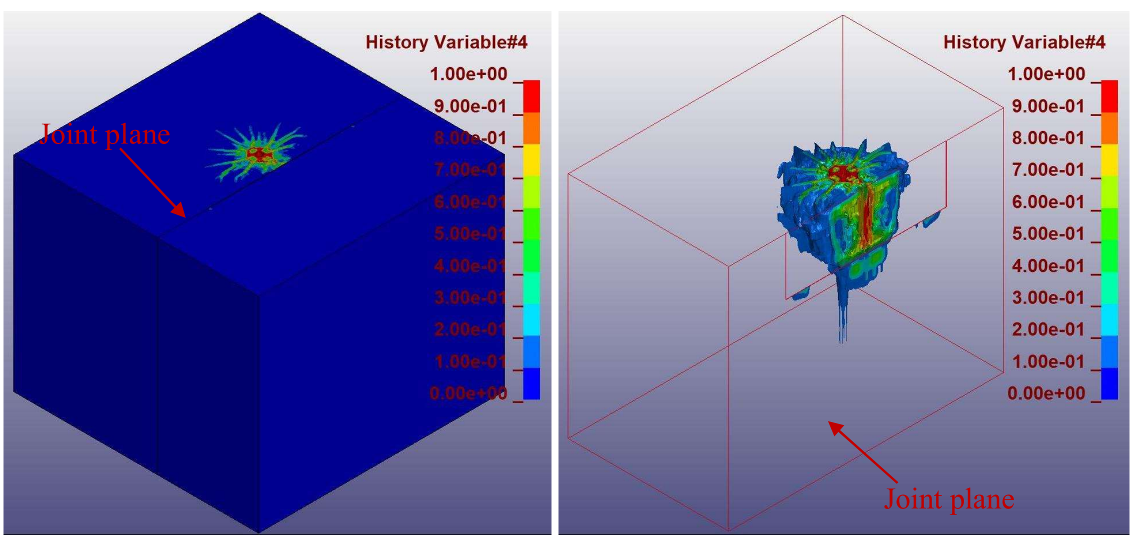

(a) (b)

Fig. 11. Blasting-induced damage pattern for case A. (a) on the top surface and (b) perspective view.

Fig. 12 compares the damage contours on the top surface and the joint plane for cases A and B. It can be clearly seen that there is no additional damage at the edges of the rock bridges in case B. This is due to very little or negligible stress concentration around the rock bridges in case B for the considered intensity of detonation. This indicates that the size of the joints has a significant influence on the expansion of the crack networks in the rock mass.

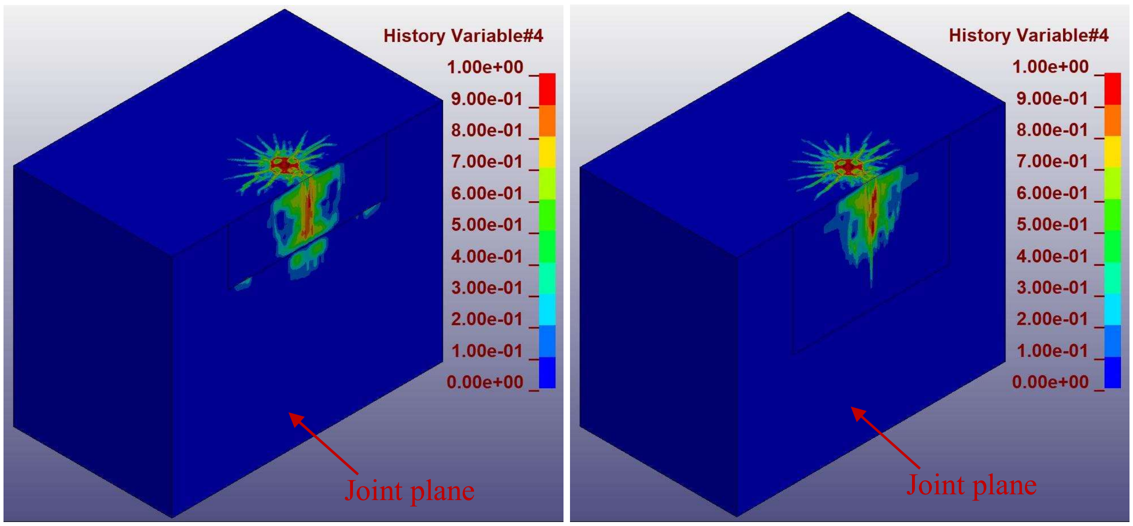

(a) (b)

Fig. 12. Crack pattern on the top surface and on the joint plane for (a) case A and (b) case B.

The fracturing patterns and damage contours for cases C and D are shown in Figs. 13 and 14. The results show that the blasting-induced damage in rock is controlled by the joint persistence as well as the spatial location of the rock bridges. There are many blasting-induced cracks can be seen in the region immediately around the joint plane in all the cases and these cracks are mainly generated by tensile failure. This is due to the blasting-induced stress wave reflects at the joint plane, and the reflected stress wave exceeds the dynamic tensile strength of the rock at these locations. Although there are no cracks beyond the joint plane in cases A and B, few new cracks were generated beyond the joint plane in cases C and D, as shown in Figs. 13(a) and 14(a). Moreover, additional damage can be seen at the edges of the rock bridges due to the envisaged significant stress concentration at these locations when the blasting-induced stress wave hits the rock bridges. This indicates that the rock bridge location has a significant influence on the expansion of the crack networks in the rock mass.

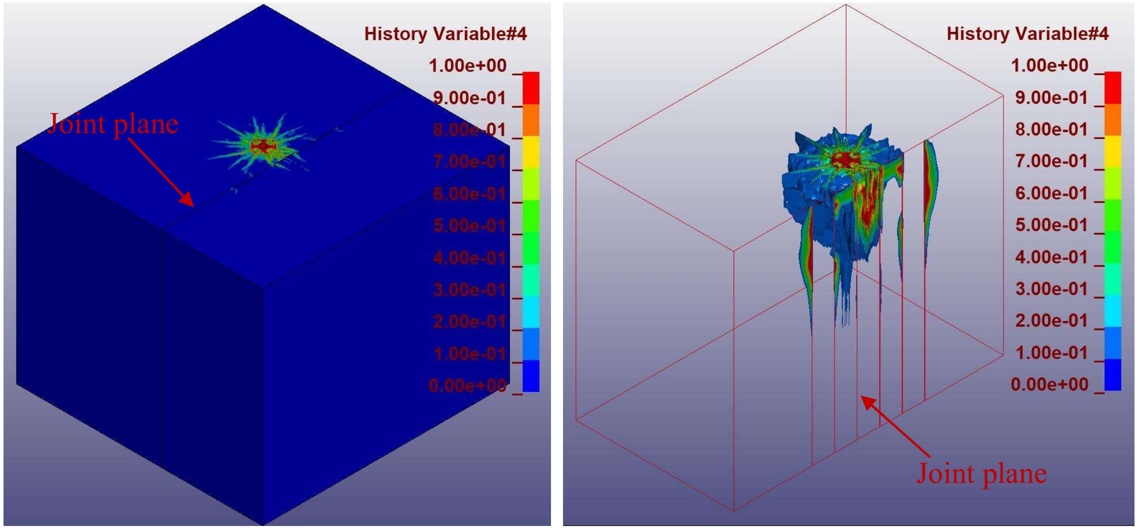

(a) (b)

Fig. 13. Crack pattern for case C. (a) on the top surface and (b) perspective view.

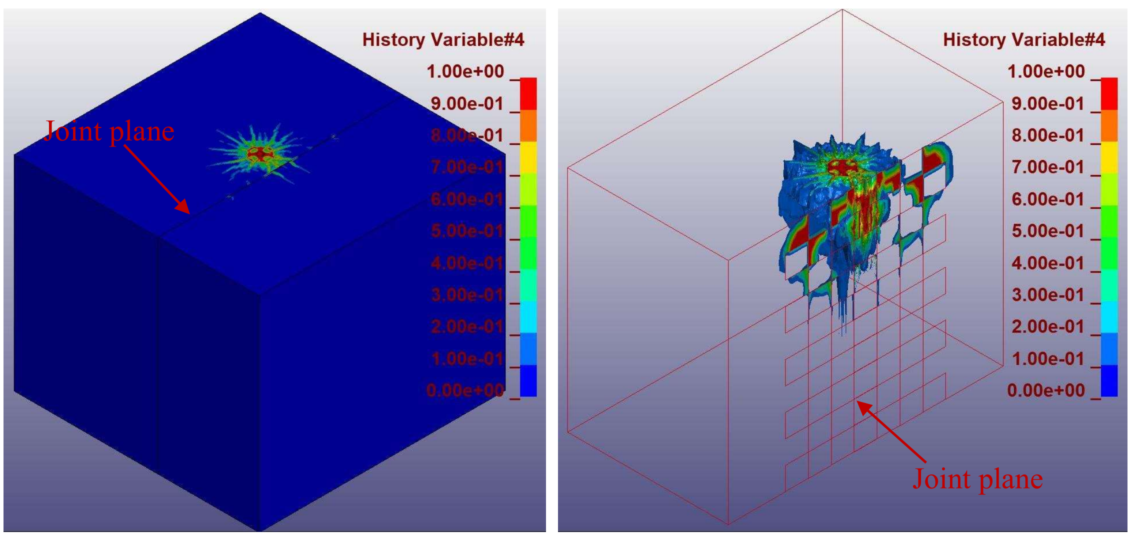

(a) (b)

Fig. 14. Crack pattern for case D. (a) on the top surface and (b) perspective view.

3.3 Fracture characteristics of rocks with different explosives

In order to investigate the effect of explosive types on fracture characteristics, three models were created with different explosives in the blasthole. The first model considers the ANFO explosive detonation in the blasthole (case 1), and the other two models include the detonation of TNT and Emulsion explosives, respectively (case 2 and 3). TNT is the most powerful explosive among them and when it explodes it releases a large amount of energy with a high velocity. For comparison, TNT, Emulsion and ANFO contain detonation energy per unit volume of 7×10^6, 3.87×10^6 and 2.484×10^6 kJ/m^3, respectively. The other important parameter to simulate the power of the detonation of the explosive is the velocity of detonation which is the speed of the detonation shock wave travels through the explosives. TNT has a detonation velocity of 6930 m/s compared to 5122 m/s for the Emulsion and 4160 m/s for ANFO. The material parameters for TNT and Emulsion explosives are described in Table 6.

Table 6. Material and JWL EOS parameters for TNT and Emulsion [14, 32]

Explosive	Density (kg/m^3)	Velocity of detonation (m/s)	P_{CJ} (GPa)	A (GPa)	B (GPa)	R_1	R_2	ω	E_0 (GPa)
TNT	1630	6930	21	371	3.23	4.15	0.95	0.3	7
Emulsion	1180	5122	9.53	276.2	8.44	5.2	2.1	0.5	3.87

Figs. 15 and 16 show the fracture patterns and damage contours obtained from the three models. By comparing the results obtained in each case, it can be seen that the top surface of the rock mass is subjected to extensive damage when TNT explosive detonated in the blasthole. On the other hand, it induced less damage below the ground surface. At depths, extensive blasting-induced damage can be seen in case 1 compared to other two cases. Furthermore, when the blasting pressure is high, the crushed zone clearly increases. Because most of energy is spent to create the crushed zone around the blasthole. In drill and blast method, blasting is considered productive when it creates long radial cracks and uniform damage along the length of blasthole. Thus, by comparing the results obtained in each case, it is clear that the use of ANFO which has low blasting pressure and velocity of detonation will help to improve the efficiency of blasting operation.

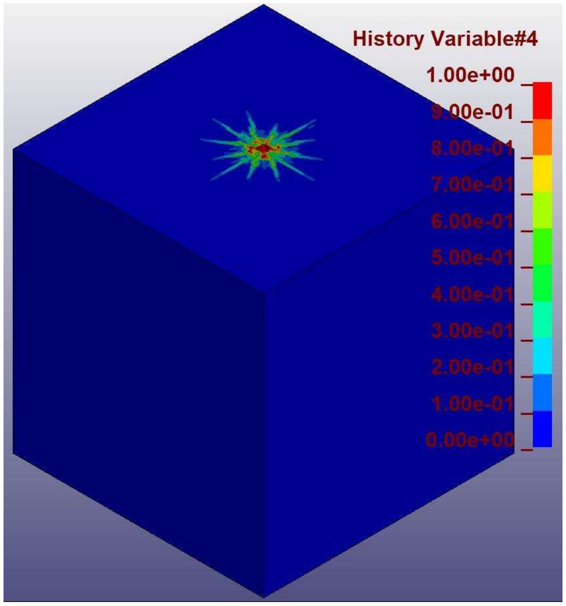

(a)

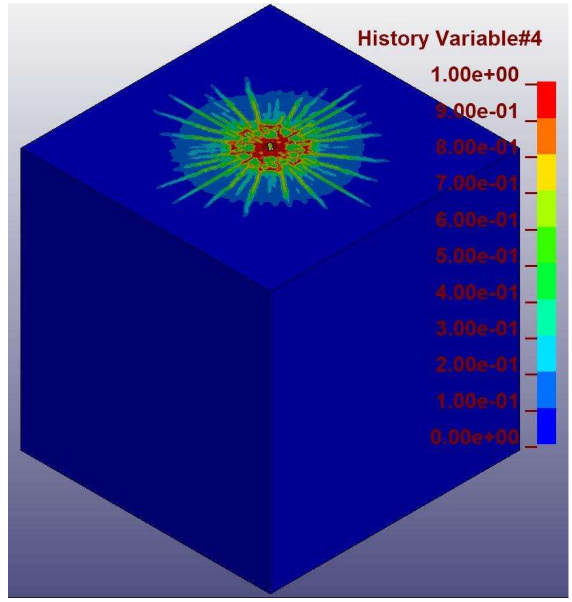

(b)

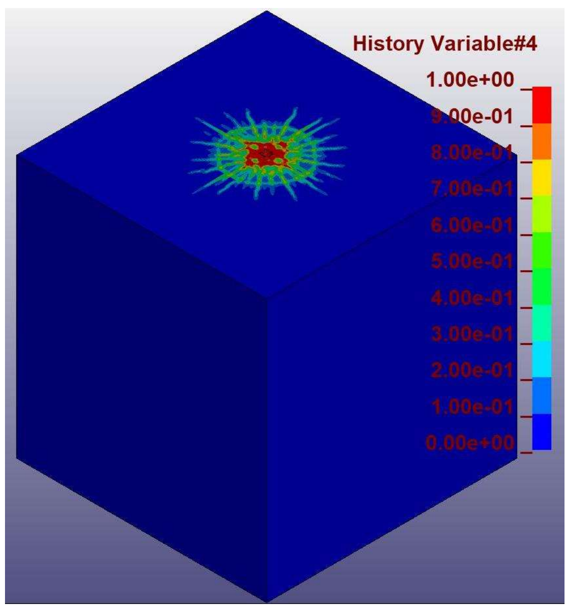

(c)

Fig. 15. Crack patterns observed on the top surface for (a) case 1 - ANFO (b) case 2 - TNT (c) case 3 - Emulsion

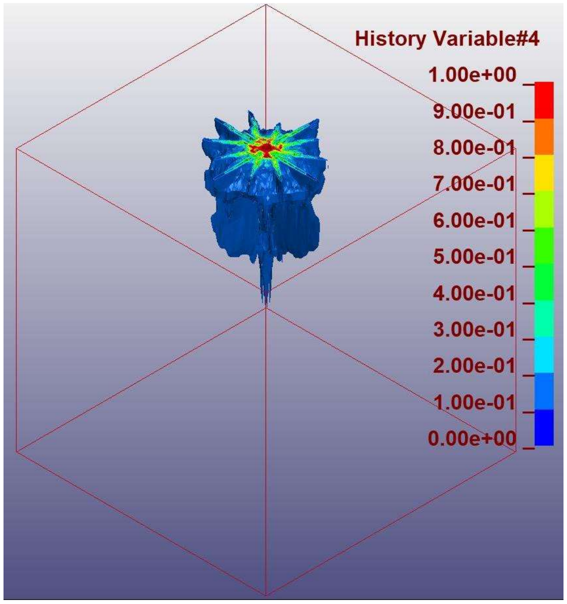

(a)

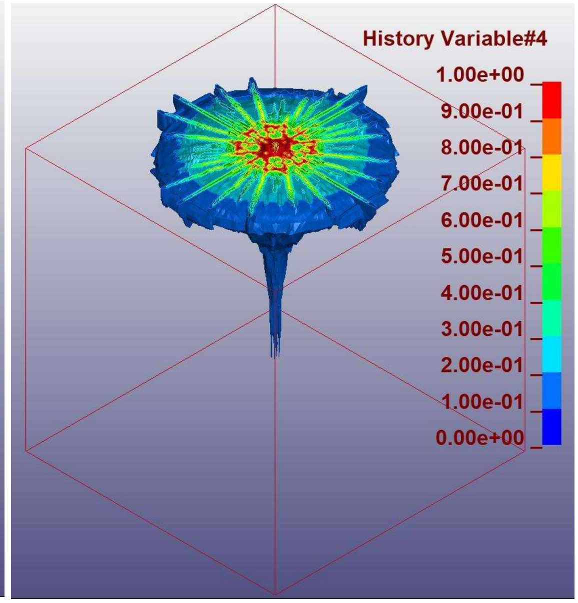

(b)

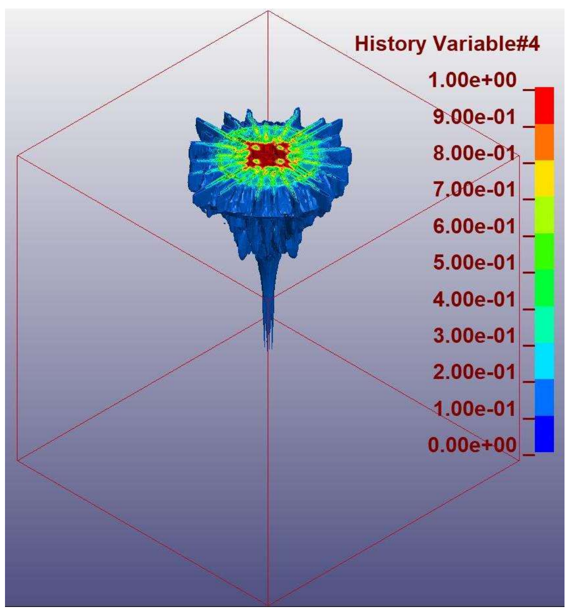

(c)

Fig. 16. Perspective view of blasting-induced rock damage for (a) case 1 - ANFO (b) case 2 - TNT (c) case 3 - Emulsion

4. Conclusion

A comprehensive numerical investigation of the effect of in-situ stress and discontinuity persistence on the blasting-induced damage characteristics of rocks was conducted based on an established 3D SPH-FEM model. Since 2D analyses cannot incorporate the three-dimensional propagation of the energy from the detonation of the explosive, the fully coupled 3D SPH-FEM model was therefore developed, which considers both computation efficiency and modeling accuracy. The model was calibrated and validated against available experimental results in literature. The effects of discontinuity persistence, high in-situ stresses, and magnitude of blast pressures on the evolution of blasting-induced damage were studied. Based on the numerical simulation results, the following conclusions can be drawn.

1. The extent of blasting-induced cracks decreases with increasing the lateral in-situ stresses. The results of this study also show that the blasting-induced cracks are oriented in the direction of the high principal stress.

2. The blasting-induced damage in the rock is controlled by the joint persistence and the location of the rock bridges. Extensive blasting-induced cracks are generated around the blastholes and in the regions around the joint planes, because the blasting-induced stress wave reflects from the top free surface and produces more tensile stress wave. When the blasting-induced stress wave hits the rock bridges, additional cracks are generated at the edges of the rock bridges due to the high stress concentration at those locations.

3. It creates a larger crushed zone when the blasting pressure is high; however, when it is low, it creates long radial cracks and uniform damage along the length of the blastholes. This means that the use of the explosive like ANFO, which has low blasting pressure and velocity of detonation, will help to improve the efficiency of blasting operation.

References

[1] S. P. Singh and P. Xavier, "Causes, impact and control of overbreak in underground excavations," *Tunnelling and Underground Space Technology,* vol. 20, pp. 63-71, 2005.

[2] H. K. Verma, N. K. Samadhiya, M. Singh, and V. V. R. Prasad, "Blast induced damage to surrounding rock mass in an underground excavation," *Journal of Geological Resource and Engineering,* vol. 2, pp. 13-19, 2014.

[3] M. F. Hossaini, M. Mohammadi, J. Ghadimi, and A. Abbasi, "Causes of overbreak in tunneling: A case study of Alborz tunnel," in *16th Coal Operators' Conference*, University of Wollongong, 2016, pp. 127-131.

[4] A. Daraei and S. Zare, "Prediction of overbreak depth in Ghalaje road tunnel using strength factor," *International Journal of Mining Science and Technology,* vol. 28, pp. 679-684, 2018.

[5] H. P. Rossamanith, K. Uenishi, and N. Kouzniak, "Blast wave propagation in rock mass - Part I: monolithic medium," *International Journal of Blasting and Fragmentation,* vol. 1, pp. 317-359, 1997.

[6] F. V. Donze, J. Bouchez, and S. A. Magnier, "Modeling fractures in rock blasting," *International Journal of Rock Mechanics and Mining Sciences,* vol. 34, no. 8, pp. 1153-1163, 1997.

[7] E. Hamdi, N. B. Romdhane, and J. M. L. Cleach, "A tensile damage model for rocks: Application to blast induced damage assessment," *Computers and Geotechnics,* vol. 38, no. 2, pp. 133-141, 2011.

[8] H. M. An, H. Y. Liu, H. Han, H. Zheng, and X. G. Wang, "Hybrid finite-discrete element modelling of dynamic fracture and resultant fragment casting and muck-piling by rock blast," *Computers and Geotechnics,* vol. 81, pp. 322-345, 2017.

[9] G. W. Ma and X. M. An, "Numerical simulation of blasting-induced rock fractures," *International Journal of Rock Mechanics and Mining Sciences,* vol. 45, pp. 966-975, 2008.

[10] Z. L. Wang and H. Konietzky, "Modelling of blast-induced fractures in jointed rock masses," *Engineering Fracture Mechanics,* vol. 76, pp. 1945-1955, 2009.

[11] Z. Zhu, H. Xie, and B. Mohanty, "Numerical investigation of blasting-induced damage in cylindrical rocks," *International Journal of Rock Mechanics and Mining Sciences,* vol. 45, pp. 111-121, 2008.

[12] O. Yilmaz and T. Unlu, "Three dimensional numerical rock damage analysis under blasting load," *Tunnelling and Underground Space Technology,* vol. 38, pp. 266-278, 2013.

[13] J.-J. Zhao, Y. Zhang, and P. G. Ranjith, "Numerical simulation of blasting-induced fracture expansion in coal masses," *International Journal of Rock Mechanics and Mining Sciences,* vol. 100, pp. 28-39, 2017.

[14] C. Yi, D. Johansson, and J. Greberg, "Effects of in-situ stresses on the fracturing of rock by blasting," *Computers and Geotechnics,* vol. 104, pp. 321-330, 2018.

[15] J. Shang, "Persistence and tensile strength of incipient rock discontinuities", PhD thesis, the University of Leeds, United Kingdom, 2016.

[16] J. Shang, S.R. Hencher, L.J. West, and K. Handley, "Forensic excavation of rock masses: a technique to investigate discontinuity persistence", *Rock Mechanics and Rock Engineering,* vol. 50, no. 11, pp. 2911-2928, 2017.

[17] LSTC, "LS-DYNA theory manual," ed. Livermore Software Technology Corporation, 2006.

[18] W. Riedel, K. Thoma, S. Hiermaier, and E. Schmolinske, "Penetration of reinforced concrete by BETA-B-500 numerical analysis using a new macroscopic concrete model for hydrocodes," in *9th International Symposium on the Effects of Munitions with Structures*, 1999.

[19] L. X. Xie, W. B. Lu, Q. B. Zhang, Q. H. Jiang, M. Chen, and J. Zhao, "Analysis of damage mechanisms and optimization of cut blasting design under high in-situ stresses," *Tunnelling and Underground Space Technology,* vol. 66, pp. 19-33, 2017.

[20] S. Jeon and T. Kim, "Characteristics of crater formation due to explosives blasting in rock mass," *Geomechanics and Engineering,* vol. 9, no. 3, pp. 329-344, 2015.

[21] K. Liu, Q. Li, C. Wu, X. Li, and J. Li, "A study of cut blasting for one-step raise excavation based on numerical simulation and field blast tests," *International Journal of Rock Mechanics and Mining Sciences,* vol. 109, pp. 91-104, 2018.

[22] T. Borrvall and W. Riedel, "The RHT concrete model in LS-DYNA," in *The 8th European LS-DYNA Users Conference*, Strasbourg, 2011.

[23] M. A. Cook, *The Science of High Explosives*. Einhold Publishing Corp, 1958.

[24] Q. Liu and P. Tidman, "Estimation of the dynamic pressure around a fully loaded blasthole," in "Technical Report MRL 95-014, CANMET/MRL:15," 1995.

[25] J. Dai, *Dynamic Behaviours and Blasting Theory of Rock*. Metallurgical Industry Press, 2002.

[26] M. M. D. Banadaki, "Stress-wave induced fracture in rock due to explosion action," Ph.D thesis, Department of Civil Engineering, University of Toronto, 2010.

[27] S. Koneshwaran, D.P. Thambiratnam, and Gallage C, " Performance of buried tunnels subjected to surface blast incorporating fluid structure interaction," *Journal of Performance of Constructed Facilities*, vol. 29, no. 3, 2014.

[28] H. H. Einstein, D. Veneziano, G. B. Baecher, and K. J. O'Reilly, "The effect of discontinuity persistence on rock slope stability," *International Journal of Rock Mechanics and Mining Sciences and Geomechanics Abstracts,* vol. 20, no. 5, pp. 227-236, 1983.

[29] J. Shang, Z. Zhao, J. Hu, and K. Handley, "3D particle-based DEM investigation into the shear behaviour of incipient rock joints with various geometries of rock bridges," *Rock Mechanics and Rock Engineering,* vol. 51, no. 11, pp. 3563-3584, 2018.

[30] B. H. Kim, M. Cai, P. K. Kaiser, and H. S. Yang, "Estimation of block sizes for rock masses with non-persistent joints," *Rock Mechanics and Rock Engineering,* vol. 40, no. 2, pp. 169-192, 2007.

[31] J. Shang, J.L. West, S.R. Hencher, and Z. Zhao, "Geological discontinuity persistence: implications and quantification," *Engineering Geology,* vol. 241, pp. 41-54, 2018.

[32] E. Lee, M. Finer, and W. Collins, JWL equation of state coefficients for high explosives, Lawrence Livermore Laboratory, University of California, 1973.